WDM PERFORMANCES OF TWO- AND THREE-WAVEGUIDE MACH-ZEHNDER SWITCHES ASSEMBLED INTO 4 × 4 MATRIX ROUTER

Giovanna Calò[*] and Vincenzo Petruzzelli

Dipartimento di Ingegneria Elettrica e dell'Informazione, Politecnico di Bari, Via Re David n. 200, Bari 70125, Italy

Abstract—The performance comparison of two configurations of broadband Mach-Zehnder Switches exploiting, respectively, two and three waveguides, assembled into 4 × 4 matrices is reported in this paper. The simulations are performed by the Finite Element Method and the Finite Difference Beam Propagation Method. In particular, we have found that, to parity of maximum insertion loss, about equal to 1 dB for the single switch and 3 dB for the 4 × 4 matrix, the proposed three-waveguide configuration exhibits an almost doubled bandwidth $\Delta\lambda = 115$ nm, making it suitable for efficient routing of the Wavelength Division Multiplexing signals over photonic Networks on Chip.

1. INTRODUCTION

Chip Multiprocessors that exploit the potentialities of parallel computing are the state of the art solution to face the constant need of increasing computing system efficiency. A chip multiprocessor consists of several smaller processing cores designed and replicated several times. They achieve performance gain through parallel code execution using multiple threads across the cores. As the number of cores in chip multiprocessors continues to scale, the efficient interconnection of these cores is becoming a major challenge to overcome the communication bottleneck, thus obtaining high bandwidth, low-power and low-latency requirements. All these characteristics cannot be matched by traditional point-to-point connections through dedicated wires. Network-on-chips (NoCs) have emerged as a technology enabling a high degree of integration in multi-core systems on chip. The NoCs were introduced to reduce the wiring complexity and to increase the

communication efficiency by designing regular topologies. However, an important performance limitation in traditional NoCs, which are mainly made by switching elements, network interfaces and inter-switch links, arises from multi-hop communications based on planar metal interconnects and to the consequent high latency and power consumption. In fact, at the physical level, the metal interconnect is responsible for depressing the on-chip data bandwidth while consuming an increasing percentage of power.

The recent developments in nanotechnology have enabled promising alternatives, such as Photonic Networks on Chip (PhNoC), which are opening new perspectives of performance improvement in Chip Multiprocessor (CMP) architectures. In fact, the integration of a photonic layer into CMPs allows to exploit the advantages of optical data transmission, such as high transmission bandwidth, low latency, low power consumption, etc. [1].

Among the components necessary for on-chip photonic communication, such as multiplexers/demultiplexers [2], multiwavelength filters [3, 4], modulators [5–9], the switches play a fundamental role for their capability of routing the signals along the network thus connecting the different processors.

A variety of technologies have been proposed for the realization of innovative and integrable photonic components useful for optical data communication such as active switches based on III-V or III-V-N compounds, which conjugate the switching functionality to the signal amplification [10–14], or devices exploiting non-linear materials, liquid crystals, or photonic crystals for multi-channel filtering and narrow-band switching [4, 15–20]. However, the silicon nanotechnology seems to be the one more mature in the context of on-chip integration, thanks to its compatibility with standard CMOS fabrication processes.

Silicon components allow the realization of reconfigurable networks due to the possibility of inducing a refractive index variation by thermo-optic or plasma-optic effects. For example, data rate up to $40\,\text{Gb/s}$ has been reached by plasma-optic effect in reversely biased p-n junctions [5–9]. Moreover, the data rate can be enhanced up to Tb/s by the implementation of Wavelength Division Multiplexing (WDM) schemes in the PhNoC.

The WDM, which allows the parallel transmission of multiple channels on the same waveguide, each associated to a different wavelength, requires the exploitation of broadband switches capable of contemporarily routing the different channels. In a previous work [21] we proposed a broadband Mach-Zehnder switch configuration based on three-waveguide couplers which guarantees a broadband operation compared to the conventional two-waveguide configuration. Here,

we discuss the performances of the switches assembled into 4×4 matrices which are the basic elements necessary to build up the entire network thus allowing the different processors to exchange sets of data. Moreover, the proposed numerical approach is useful for the integration of the photonic switching elements into network design tools. In fact, on one hand the optimization of the overall photonic NoC requires the simulation of the network architecture by dedicated tools [22], which can not simulate the optical devices at a physical level. On the other hand, the design of SOI switches needs complex numerical models based on the differential equations for accounting the physical phenomena, such as the carrier dynamics and the electromagnetic propagation. An accurate analysis of the physical phenomena underlying the switching element functionality, allows for describing the optical devices through equivalent black-boxes to be included into the models at the network level.

In this paper, we report the results of the design and the simulations of two configurations of broadband Mach-Zehnder Switch (MZS) exploiting, respectively, two and three waveguides. The switches are based on SOI waveguides assembled into Mach-Zehnder interferometric configurations in which the phase shift is induced by the plasma-optic effect. The simulation of the carrier dynamics was performed by the Finite Element Method (FEM) [23, 24], whereas the electromagnetic propagation was simulated through the Finite Difference Beam Propagation Method (FD-BPM) [25]. By means of these numerical models we obtain the switch transmittance and other relevant parameters, such as the insertion loss and the power consumption, necessary for the black-box description of the devices at the network simulation level. Finally, the performances of the two MZSs assembled into 4×4 switch matrices are evaluated.

2. TWO AND THREE-WAVEGUIDE MACH-ZEHNDER SWITCHES

The designed reconfigurable Mach-Zehnder switches are schematized in Figure 1. They are made of two 50% coupling sections, exploiting two (Figure 1(a)) or three (Figure 1(b)) waveguide couplers and of a phase shifter region in which a π phase shift is achieved by plasma-optic effect in a forward biased p-i-n junction. In both the cases, the signal launched at port 1 is completely transferred at port 4 when no plasma-optic effect is considered (OFF$_1$ state), whereas it is transferred at port 3 (ON$_1$ state) thanks to the plasma-optic effect and to the consequent change in carrier concentration, which induces a π phase shift between the active and the reference arms of the MZS. Similar
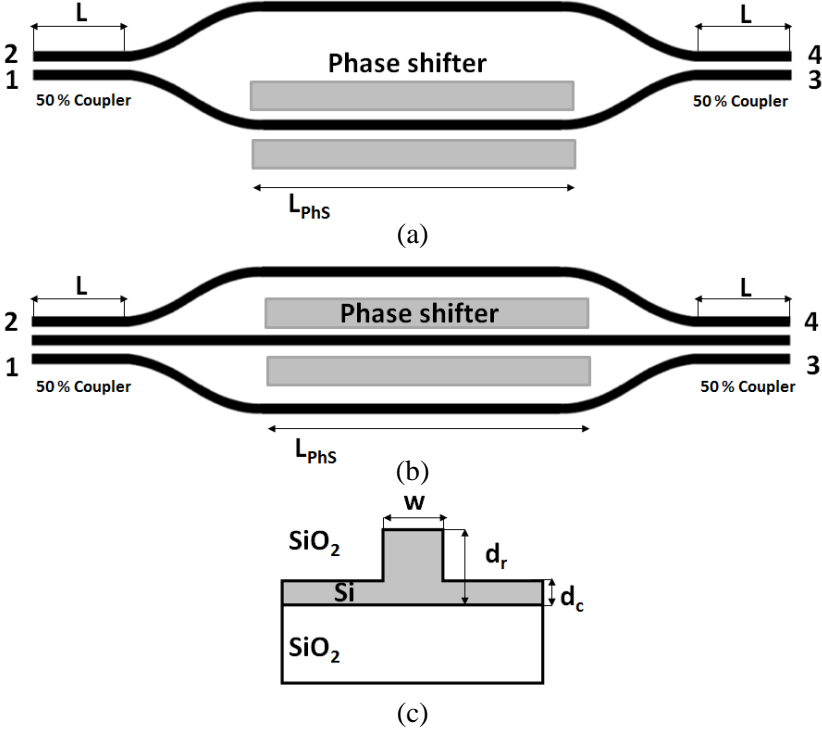
Figure 1. Scheme of the (a) two- and (b) three-waveguide MZSs made of two 50% coupling sections and of a phase shifting region. The transversal section of the rib waveguide (c) constituting the MZ is shown, too. In both the configurations, the optical signal launched at port 1 (port 2) is transmitted at port 4 (port 3) in the OFF state, whereas in the ON state it is transmitted at port 3 (port 4).

behaviour occurs for the input signal launched at port 2. In this case, the input signal is transferred to port 3 in the OFF_2 state and to port 4 in the ON_2 state.

The waveguides, whose cross section is shown in Figure 1(c), are silicon ribs embedded in SiO_2 having core thickness $d_c = 0.05\,\mu m$, rib thickness $d_r = 0.20\,\mu m$, rib width $w = 0.50\,\mu m$, silicon and silicon dioxide refractive indices $n_{Si} = 3.477$ and $n_{SiO_2} = 1.444$, respectively, at the wavelength $\lambda = 1.55\,\mu m$. The separation gap between the coupled waveguides is equal to $0.30\,\mu m$. In the phase shifter region, a forward biased p-i-n diode is formed by the intrinsic silicon core and by two highly doped p^+ and n^+ regions, having carrier density $N_e = N_h = 10^{20}\,cm^{-3}$.

The refractive effective index change and the losses induced by the free-carrier plasma dispersion effect depends on the variation of the electron and hole distributions. The FEM is an efficient and accurate numerical technique to solve partial differential equations or systems modelling physical phenomena essential to investigate a wide spectrum of optical components. FEM transforms a very complicated problem into small elements, each solved in relation to the other, by approximating each element with suitable polynomial approximation functions. In substance, the procedure consists of eliminating the spatial derivatives by reducing the partial differential equation in a system of algebraic equations for steady state problems and in a system of ordinary differential equations for transient problems. Recently, the FEM technique has been efficiently applied to different architectures of silicon plasma dispersion modulators. In fact, the electron and the hole distribution can be easily calculated either in static analysis or dynamic analysis by using the FEM to solve the 2-D drift-diffusion equation [23, 24]. Then, from the 2-D free-carrier distribution, silicon refractive index and absorption coefficient changes due to applied voltage are calculated using the well-known Soref-Bennett formulas [26].

The calculated average silicon refractive index change Δn and the loss coefficient α are $\Delta n = -5.282 \cdot 10^{-3}$ and $\alpha = 27.80\,\mathrm{cm}^{-1}$, respectively, for an applied voltage $V = 1\,\mathrm{V}$. According to the refractive index variation, the length of the phase shifting region $L_{PhS} = 147.54\,\mathrm{\mu m}$ was chosen to achieve the required π phase shift at the wavelength $\lambda = 1.55\,\mathrm{\mu m}$. Moreover, a power consumption of $2.6\,\mathrm{mW}$ and a switching time $t_s \cong 4\,\mathrm{ns}$ were evaluated by means of the FEM time dependent simulations.

Once the 2-D distribution of refractive index and absorption coefficient is known, the electromagnetic field distribution along the switch has been evaluated by the FD-BPM, which is a numerical method suitable for the analysis of strongly guiding structures. By the FD-BPM the Helmholtz wave equation:

$$\nabla^2 E(x, y, z) + k_0^2 n^2(x, y, z)E(x, y, z) = 0 \qquad (1)$$

is solved by applying a finite-difference scheme by which the continuous 3-D space is discretized into a grid defined in the computation region, thus reducing the wave Equation (1) to an algebraic system. In Equation (1) k_0 is the wavenumber in vacuum and $n(x, y, z)$ is the refractive index of the structure. A split-step algorithm was used to optimize the computation time and the transparent boundary conditions were introduced to absorb the waves outgoing from the computation window. In order to evaluate the performances of the conventional 2WG MZS and of the proposed 3WG MZS, we consider

two figures of merit, i.e., the crosstalk CT and the insertion loss IL, calculated according to the following formulas:

$$CT_{ij} = 10 \cdot \log_{10}\left(T_i/T_j\right) \qquad (2)$$
$$IL_{ij} = 10 \cdot \log_{10}\left(1/T_j\right) \qquad (3)$$

where T_i and T_j are the transmittances at the ports i and j when the signal is launched in input at the same waveguide corresponding to the port i.

Owing to the refractive index dispersion, the switch performances worsen as the operating wavelength is detuned from the design value, i.e., $\lambda = 1.55\,\mu$m. Therefore, a spectral analysis is required to evaluate the switch bandwidth, defined as the wavelength range in which the crosstalk CT and the insertion loss IL are both below the reference values $CT_R = -15\,$dB and $IL_R = 1.1\,$dB, respectively [21, 27].
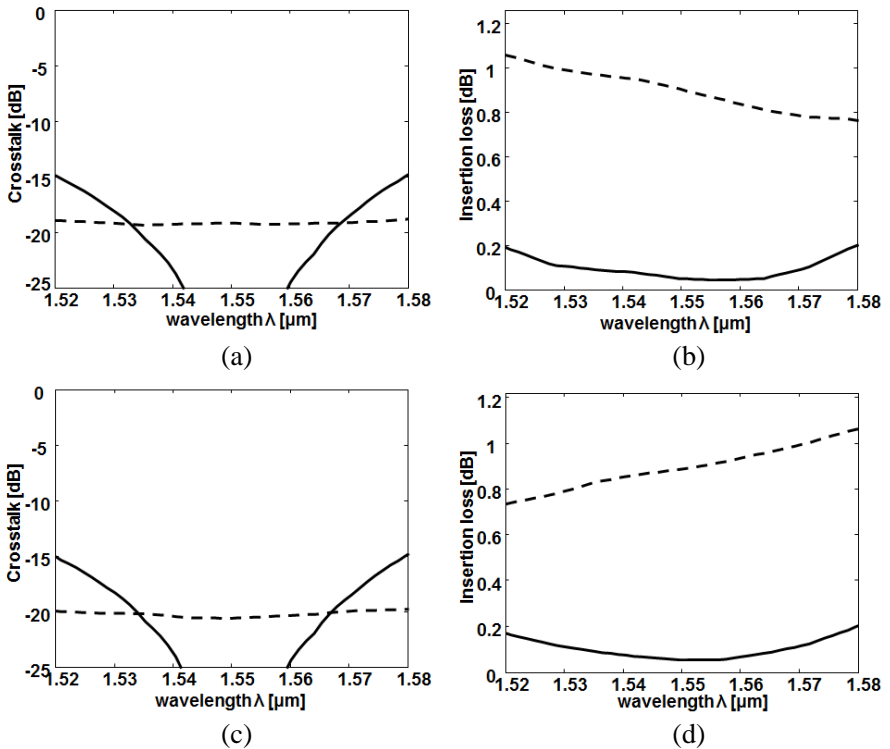

Figure 2. Crosstalk and insertion loss in the OFF (solid curves) and ON (dashed curves) states for the 2WG MZS with input signal launched (a) (b) at port 1 and (c) (d) at port 2.
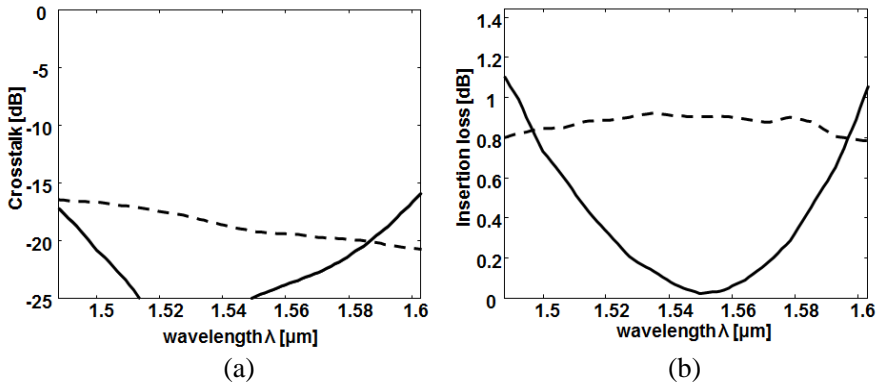
Figure 3. (a) Crosstalk and (b) insertion loss in the OFF (solid curves) and ON (dashed curves) states for the 3WG MZS.

Figure 2 shows the crosstalk and the insertion loss in the wavelength range where both the conditions $CT < -15\,\text{dB}$ and $IL < 1.1\,\text{dB}$ are fulfilled, for the 2WG MZS in the OFF (solid curves) and in the ON (dashed curves) states. In particular, Figures 2(a) and (b) refer to the case of input signal launched at port 1, whereas Figures 2(c) and (d) refer to the case of input signal launched at port 2.

Since the 2WG-MZS becomes asymmetric in the ON state (dashed curves), owing to the refractive index change in the phase shifter, the CT and the IL spectra calculated when the input signal is launched at port 1 (Figures 2(a) and (b)) are slightly different from those calculated when the input signal is launched at port 2 (Figures 2(c) and (d)).

Figure 3 shows the crosstalk (Figure 3(a)) and the insertion loss (Figure 3(b)) for the 3WG MZS in the OFF (solid curves) and in the ON (dashed curves) states in the wavelength range where both the conditions $CT < -15\,\text{dB}$ and $IL < 1.1\,\text{dB}$ are fulfilled. In this case, the spectral behavior of the 3WG MZS remains unchanged either when the input signal is launched at port 1 or at port 2, since the device is anyway symmetric.

We have calculated that the MZS bandwidth is equal to $\Delta\lambda = 60\,\text{nm}$ and $\Delta\lambda = 115\,\text{nm}$ in the cases of two- and three-waveguide configurations, respectively. Therefore, the three-waveguide MZS exhibits an almost doubled bandwidth useful for the WDM transmission on optical NoCs.
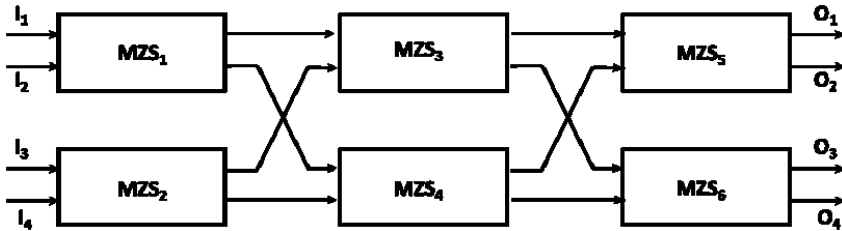
Figure 4. Black box scheme of the 4×4 switch matrix.

3. 4×4 MACH-ZEHNDER SWITCH MATRIX

The above-mentioned analysis, through the combination of the FEM drift-diffusion model and the FD-BPM model of the electromagnetic propagation, provides a description at the physical level of the MZSs which characterizes the device behavior at the ports (as shown in Figures 2 and 3). From the knowledge of these spectra it is possible to consider the MZSs as black boxes that allow the implementation of reliable numerical models at the network level.

In this way, the behavior of the switch matrixes and of the overall network can be predicted by suitably multiplying the transfer functions according to the switch connections within the network.

As schematized in Figure 4, we focus on the analysis of a 4×4 switch matrix in which six MZSs are connected according to the Benes configuration [28]. We have chosen this classical and simple configuration of switch matrix to compare the performances of the conventional 2WG MZS with those of the proposed 3WG MZS. However, for more efficient and more complex configurations the analysis would be similar [27].

Table 1 reports the eight states of the switch matrix that allow the connection of each input port I_i, $i = 1, 2, 3, 4$ with all the output ports O_j, $j = 1, 2, 3, 4$, with two different paths. The ON and OFF conditions, denoted respectively by 1 and 0, are also reported in Table 1 for the six MZSs.

Each signal path, connecting the input I_i with the output O_j, involves three MZSs which can be either in the ON or in the OFF conditions. As an example, when the switch matrix is in the state 1, that is MZS_1 and MZS_5 in OFF condition and the other ones in the ON condition, the input port I_i is directly linked to the output port O_i, for $i = 1, 2, 3, 4$. Therefore, for example, the signal launched at port I_1 will be transmitted at port O_1 passing through the switches MZS_1, MZS_4, and MZS_5 which are in the OFF, ON, and OFF conditions,

Table 1. Eight states of the 4×4 switch matrix with the corresponding ON and OFF conditions, denoted respectively by 1 and 0, for the six MZSs and the input/output paths.

State	ON/OFF conditions for the MZSs						I/O paths			
	MZS_1	MZS_2	MZS_3	MZS_4	MZS_5	MZS_6	I_1	I_2	I_3	I_4
1	0	1	1	1	0	1	O_1	O_2	O_3	O_4
2	0	0	1	1	1	1	O_2	O_1	O_4	O_3
3	0	1	0	0	1	0	O_3	O_4	O_1	O_2
4	0	1	0	1	0	1	O_4	O_3	O_2	O_1
5	1	0	1	1	1	0	O_1	O_2	O_3	O_4
6	1	1	1	1	0	1	O_2	O_1	O_4	O_3
7	1	0	0	0	0	1	O_3	O_4	O_1	O_2
8	1	0	0	0	1	0	O_4	O_3	O_2	O_1

respectively. On the other hand, the signal launched at the port I_2 will emerge from the port O_2 through MZS_1, MZS_3, and MZS_5, in the OFF, ON, and OFF conditions, respectively. Similar behavior occurs for the other two links $I_3 \rightarrow O_3$ and $I_4 \rightarrow O_4$.

In the evaluation of the switch matrix performance, the most relevant parameter is the insertion loss. In fact, the cascade of multiple devices does not significantly change the crosstalk CT, calculated as the ratio between the transmittances at the switch output ports. Conversely, the total insertion loss is the sum in dB of the IL contributions of the three MZSs encountered by the signal along the generic path.

Figures 5 and 6 show the IL spectra for the 2WG-MZS (Figure 5) and for the 3WG-MZS (Figure 6) configurations assembled into 4×4 switch matrix calculated at the four output ports O_1 (solid curve), O_2 (dashed curve), O_3 (dotted curve), and O_4 (dash-dotted curve) when the input signal is launched at: (a) I_1, (b) I_2, (c) I_3, and (d) I_4 input ports.

The IL curves reported in Figures 5 and 6, calculated by Equation (3) from the FD-BPM transmittance spectra, correspond to the states from 1 to 4 in Table 1. The spectra in Figures 5 and 6 are limited to the MZS bandwidth in the case of the two- and the three-waveguide configurations, respectively.

We can see that the IL spectra change according to the signal path and to the switching condition of the three switches encountered by the signals along the paths. In particular, in the case of 2WG-MZS matrix, the loss is minimum when all the three MZSs are in the OFF condition along the path, i.e., when the signal is launched at port I_1
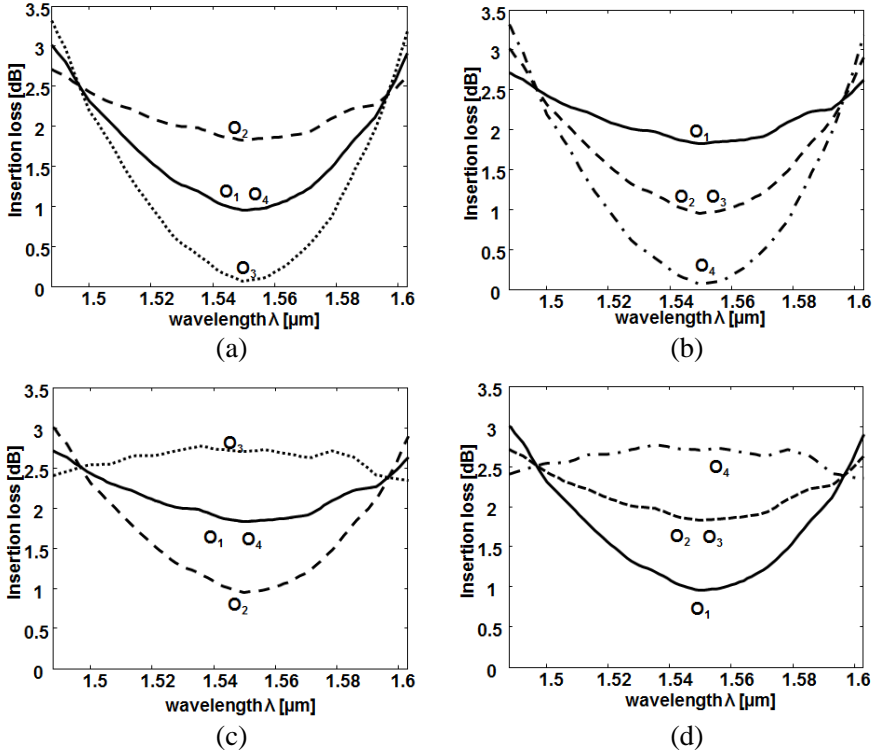
Figure 5. Spectra of the insertion loss IL for the 4×4 matrix made by 2WG-MZS calculated at the four output ports O_1 (solid curve), O_2 (dashed curve), O_3 (dotted curve), and O_4 (dash-dotted curve) when the input signal is launched at: (a) I_1 input port, (b) I_2 input port, (c) I_3 input port, and (d) I_4 input port.

and collected at port O_3 (dotted curve in Figure 5(a)) or when it is launched at port I_2 and collected at port O_4 (dash-dotted curve in Figure 5(b)). In fact, as shown in Figure 2 (b), the insertion loss is lower for the 2WG-MZS in the OFF state, whereas in the ON state the loss is higher, due to the propagation losses induced in the phase shifter by the plasma-optic effect.

In the case of the 3WG-MZS switch matrix, most of the signal paths are characterized by a maximum value of the IL at the edges of the considered wavelength range and a minimum value at the central wavelength $\lambda = 1.55\,\mu$m. This behavior is due to the presence of at least one MZS in the OFF state along the considered paths. In fact, in the case of a single 3WG-MZS switch in the ON state, as shown
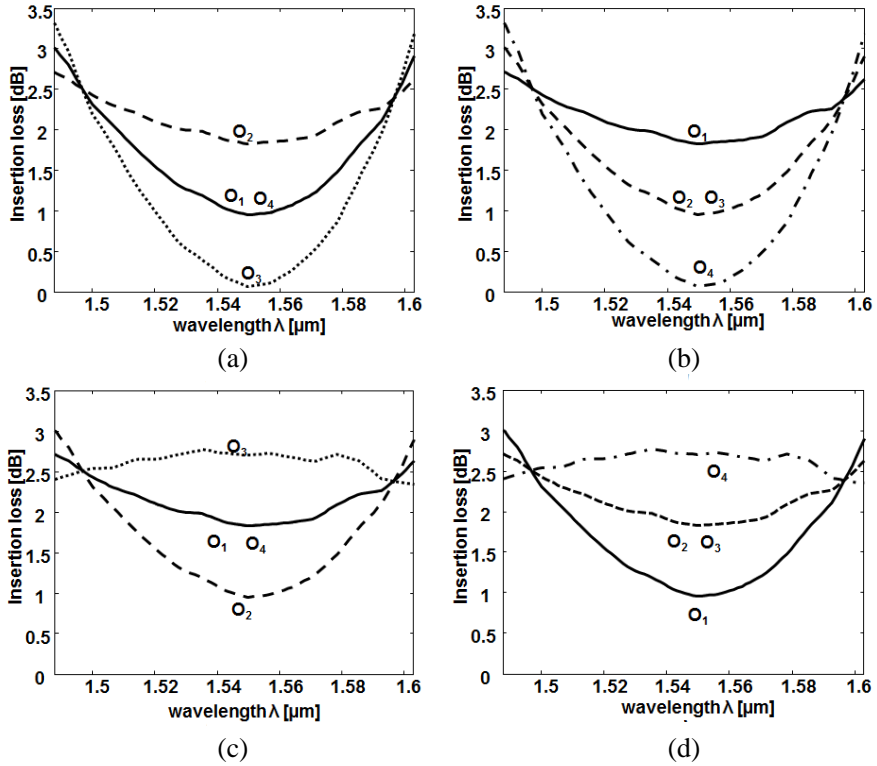
Figure 6. Spectra of the insertion loss IL for the 4×4 matrix made by 3WG-MZS calculated at the four output ports O_1 (solid curve), O_2 (dashed curve), O_3 (dotted curve), and O_4 (dash-dotted curve) when the input signal is launched at: (a) I_1 input port, (b) I_2 input port, (c) I_3 input port, and (d) I_4 input port.

in Figure 3(b) (dashed curve), the insertion loss spectrum is almost constant, whereas in the OFF state (solid curve in Figure 3(b)) it is maximum at the edges of the considered wavelength range, reaching its minimum value at the central wavelength $\lambda = 1.55 \, \mu\mathrm{m}$. This loss mechanism is mainly due to the part of the signal remaining in the central waveguide when the wavelength is detuned from the operation value $\lambda = 1.55 \, \mu\mathrm{m}$.

Moreover, from Figure 6 we can see that only the signal paths with all the three MZSs in the ON state are characterized by an almost constant trend of the IL spectrum, i.e., the paths connecting ports I_3 with O_3 (dotted curve in Figure 6(c)) and port I_4 with O_4 (dash-dotted

Table 2. Maximum insertion loss IL [dB] for different inputs I_i and outputs O_j in the case of 4×4 2WG-MZS switch matrix. The MZSs, which are in the ON state to allow the optical signal to be routed from input I_i to output O_j, are also reported.

OUT IN	O_1	O_2	O_3	O_4
I_1	MZS_4 1.44	MZS_4, MZS_5 2.06	- 0.61	MZS_6 1.46
I_2	MZS_3, MZS_5 2.27	MZS_3 1.42	MZS_6 1.42	- 0.61
I_3	MZS_2, MZS_5 2.29	MZS_2 1.41	MZS_2, MZS_3, MZS_6 2.84	MZS_4, MZS_6 2.32
I_4	MZS_2 1.46	MZS_2, MZS_5 2.33	MZS_3, MZS_6 2.89	MZS_2, MZS_4, MZS_6 3.18

Table 3. Maximum insertion loss IL [dB] for different input I_i and output O_j conditions in the case of 4×4 3WG-MZS switch matrix. The MZSs, which are in the ON state to allow the optical signal to be routed from input I_i to output O_j, are also reported.

OUT IN	O_1	O_2	O_3	O_4
I_1	MZS_4 3.01	MZS_4, MZS_5 2.70	- 3.32	MZS_6 3.01
I_2	MZS_3, MZS_5 2.70	MZS_3 2.30	MZS_6 2.30	- 3.32
I_3	MZS_2, MZS_5 2.70	MZS_2 2.30	MZS_2, MZS_3, MZS_6 2.77	MZS_4, MZS_6 2.70
I_4	MZS_2 3.01	MZS_2, MZS_5 2.70	MZS_3, MZS_6 2.70	MZS_2, MZS_4, MZS_6 2.77

curve in Figure 6(c)). In these cases, the dominant loss mechanism is the plasma-optic effect in the phase shifter.

To better compare the performances of the 2WG-MZS and of the 3WG-MZS matrices, we report in Tables 2 and 3 the maximum insertion loss for the different inputs I_i and outputs O_j corresponding to the curves in Figures 5 and 6. The Tables 2 and 3 also specify the MZSs being in the ON state along the signal path from the input I_i to the output O_j.

As reported in Table 2, in the case of 2WG-MZS matrix, the maximum insertion loss assumes the lowest value $IL = 0.61$ dB for all the switches along the path in the OFF state (i.e., from port I_1 to port O_3 and from port I_2 to port O_4), whereas the maximum insertion loss assumes the greatest value $IL = 3.18$ dB for the three switches

in the ON state. Conversely, as reported in Table 3, in the case of the 3WG-MZS matrix all the possible paths from port I_i to port O_j have comparable losses, reaching a maximum insertion loss value $IL = 3.32 \, \text{dB}$.

Although the 2WG-MZS matrix exhibits some lower-loss signal paths, the maximum IL is comparable to that of the 3WG-MZS matrix. Therefore, to parity of maximum insertion loss and, consequently, of required input optical power, the 3WG-MZS configuration is considerably advantageous in terms of bandwidth. In fact, the three-waveguide configuration exhibits a bandwidth equal to $\Delta\lambda = 115 \, \text{nm}$, whereas the bandwidth of the two-waveguide one is equal to $\Delta\lambda = 60 \, \text{nm}$. Therefore, to parity of maximum insertion loss, considering a WDM channel spacing of 2 nm, 30 channels can be allocated in the 60-nm bandwidth of the two-waveguide MZS, whereas 57 channels can be allocated in the 115-nm bandwidth of the three-waveguide one.

Moreover, if the data rate of each transmission channel is assumed equal to 10 Gb/s, the overall data rate achievable with the 2WG-MZS matrix is 300 Gb/s, whereas it becomes 570 Gb/s for the three-waveguide configuration. This is a considerable increase in the transmission data rate which leads also to an improvement of the power efficiency in terms of energy per bit, owing to the increased number of WDM channels that can be contemporarily routed to parity of switching power [28]. In fact, the power consumption depends only on the phase shifter operation which is the same for both the two- and the three-waveguide configurations. As estimated by the FEM model, the power required by a single switch in the ON state is 2.6 mW which corresponds to an energy per bit value for the two- and three-waveguide configurations equal to 8.7 fJ/b and 4.6 fJ/b, respectively.

4. CONCLUSIONS

A three-waveguide Mach-Zehnder switch configuration was proposed and analyzed through numerical simulations based on the FEM and FD-BPM models. These numerical models are used to obtain the relevant parameters necessary for the modelling and the simulation of the devices at the network level.

Compared to the conventional two-waveguide configuration, the proposed switch shows an almost doubled bandwidth thus giving enhanced performances for the WDM transmission in photonics networks on chip. In particular, considering a WDM channel spacing of 2 nm, 57 channels can be allocated in the 115-nm bandwidth of the three-waveguide MZS, whereas 30 channels are allowed in the 60-nm bandwidth of the two-waveguide conventional configuration.

This behavior also leads to an improvement of the switch efficiency in terms of energy-per-bit which is equal to 8.7 fJ/b and 4.6 fJ/b for the two- and the three-waveguide configurations, respectively. Moreover, considering the arrangement of the two MZS configurations into 4×4 switch matrixes, the overall insertion losses were evaluated showing that the maximum insertion losses are comparable in the two cases (i.e., $IL = 3.18$ dB and $IL = 3.38$ dB, respectively, for the 2WG-MZS and 3WG-MZS assembled into 4×4 switch matrixes).

ACKNOWLEDGMENT

REFERENCES

1. Biberman, A. and K. Bergman, "Optical interconnection networks for high-performance computing systems," *Rep. Prog. Phys.*, Vol. 75, 046402, 2012.

2. Kumar, A., B. Suthar, V. Kumar, K. S. Singh, and A. Bhargava, "Tunable wavelength demultiplexer for DWDM application using 1-D photonic crystal," *Progress In Electromagnetics Research Letters*, Vol. 33, 27–35, 2012.

3. Wu, C.-J., M.-H. Lee, W.-H. Chen, and T.-J. Yang, "A mid-infrared multichanneled filter in a photonic ceystal heterostructure containing negative-permittivity materials," *Journal of Electromagnetic Waves and Applications*, Vol. 25, No. 10, 1360–1371, 2011.

4. Calò, G., A. Farinola, and V. Petruzzelli, "Equalization in photonic bandgap multiwavelength filters by the Newton binomial distribution," *Journal of the Optical Society of America B*, Vol. 28, 1668–1679, 2011.

5. Green, W. M. J., M. J. Rooks, L. Sekaric, and Y. A. Vlasov, "Ultra-compact, low RF power, 10 Gb/s silicon Mach-Zehnder modulator," *Opt. Express*, Vol. 15, 17106–17113, 2007.

6. Xu, Q., S. Manipatruni, B. Schmidt, J. Shakya, and M. Lipson, "12.5 Gbit/s carrier-injection-based silicon microring silicon modulators," *Opt. Express*, Vol. 15, 430–436, 2007.

7. Liao, L., D. Samara-Rubio, M. Morse, A. Liu, and D. Hodge, "High speed silicon Mach-Zehnder modulator," *Opt. Express*, Vol. 13, 3130–3135, 2005.

8. Liu, A., L. Liao, D. Rubin, H. Nguyen, B. Ciftcioglu, Y. Chetrit, N. Izhaky, and M. Paniccia, "High-speed optical modulation based on carrier depletion in a silicon waveguide," *Opt. Express*, Vol. 15, 660–668, 2007.

9. Thomson, D. J., F. Y. Gardes, Y. Hu, G. Mashanovich, M. Fournier, P. Grosse, J.-M. Fedeli, and G. T. Reed, "High contrast 40 Gbit/s optical modulation in silicon," *Opt. Express*, Vol. 19, 11507–11516, 2011.

10. Calò, G., V. Petruzzelli, L. Mescia, and F. Prudenzano, "Study of gain in photonic band gap active InP waveguides," *Journal of the Optical Society of America B*, Vol. 26, 2414–2422, 2009.

11. Calò, G., A. D'Orazio, M. Grande, V. Marrocco, and V. Petruzzelli, "Active InGaAsP/InP photonic bandgap waveguides for wavelength-selective switching," *IEEE Journal of Quantum Electronics*, Vol. 47, No. 2 172–181, 2011.

12. Calò, G., D. Alexandropoulos, and V. Petruzzelli, "Active photonic band-gap switch based on GaInNAs multiquantum well," *IEEE Photonics Journal*, Vol. 4, No. 5, 1936–1946, 2012.

13. Calò, G., D. Alexandropoulos, and V. Petruzzelli, "Active WDM filter on dilute nitride quantum well photonic band gap waveguide," *Progress In Electromagnetics Research Letters*, Vol. 35, 37–49, 2012.

14. Calò, G., D. Alexandropoulos, A. D'Orazio, and V. Petruzzelli, "Wavelength selective switching in dilute nitrides multi quantum well photonic band gap waveguides" *Physica Status Solidi B*, Vol. 248, 1212–1215, 2011.

15. Ghafoori-Fard, H., M. J. Moghimi, and A. Rostami, "Linear and nonlinear superimposed Bragg grating: A novel proposal for all-optical multi-wavelength filtering and switching," *Progress In Electromagnetics Research*, Vol. 77, 243–266, 2007.

16. D'Alessandro, A., F. Campoli, P. Maltese, G. Chessa, A. D'Orazio, and V. Petruzzelli, "Design of an ultrashort directional coupler with an SSFLC coupling layer," *Molecular Crystals and Liquid Crystals*, Vol. 320, 355–364, 1998.

17. Moghimi, M. J., H. Ghafoori-Fard, and A. Rostami, "Analysis

and design of all-optical switching in apodized and chirped Bragg gratings," *Progress In Electromagnetics Research B*, Vol. 8, 87–102, 2008.

18. Moghimi, M. J., H. G. Fard, and A. Rostami "Multi-wavelengths optical switching and tunable filters using dynamic superimposed photorefractive Bragg grating," *Progress In Electromagnetics Research C*, Vol. 3, 129–142, 2008.

19. Calò, G., A. D'Orazio, M. De Sario, L. Mescia, V. Petruzzelli, and F. Prudenzano, "Tunability of photonic band gap notch filters," *IEEE Transactions on Nanotechnology*, Vol. 7, 273–284, 2008.

20. D'Orazio, A., M. De Sario, V. Ingravallo, V. Petruzzelli, and F. Prudenzano, "Infiltrated liquid crystal photonic bandgap devices for switching and tunable filtering," *Fiber and Integrated Optics*, Vol. 22, No. 3, 161–172, 2003.

21. Calò, G., A. D'Orazio, and V. Petruzzelli, "Broadband Mach-Zehnder switch for photonic networks on chip," *Journal of Lightwave Technology*, Vol. 30, No. 7, 944–952, 2012.

22. Parini, A., L. Ramini, G. Bellanca, and D. Bertozzi, "Abstract modeling of switching elements for optical networks-on-chip with technology platform awareness," *INA-OCMC: 5th International Workshop on Interconnection Network Architecture: On-Chip, Multi-Chip*, 2011.

23. Passaro, V. M. N. and F. Dell'Olio, "Scaling and optimization of MOS optical modulators in nanometer SOI waveguides," *IEEE Transactions on Nanotechnology*, Vol. 7, 401–408, 2008.

24. Calò, G. and V. Petruzzelli, "Photonic interconnects for chip multiprocessing architectures" *2012 14th International Conference on Transparent Optical Networks (ICTON)*, 1–4, July 2–5, 2012.

25. Huang, W., C. Xu, S. Chu, and S. K. Chaudhuri, "The finite-difference vector beam propagation method: Analysis and assessment," *J. Lightw. Technol.*, Vol. 10, 295–305, 1992.

26. Soref, R. and B. R. Bennett, "Electrooptical effects in silicon," *IEEE Journal of Quantum Electronics*, Vol. 23, 123–129, 1987.

27. Yang, M., W. M. J. Green, S. Assefa, J. Van Campenhout, B. G. Lee, C. V. Jahnes, F. E. Doany, C. L. Schow, J. A. Kash, and Y. A. Vlasov, "Non-blocking 4×4 electro-optic silicon switch for on-chip photonic networks," *Opt. Express*, Vol. 19, 47–54, 2011.

28. Thompson, R. A. and D. K. Hunter, "Elementary photonic switching modules in three divisions," *IEEE Journal of Selected Areas in Communications*, Vol. 14, No. 2, 362–372, 1996.